CRYSTAL GROWTH & DESIGN

Article

Cite This: Cryst. Growth Des. 2020, 20, 600−607

pubs.acs.org/crystal

Controlled Formation and Growth Kinetics of Phase-Pure, Crystalline $BiFeO_3$ Nanoparticles†

Alex J. Freitas Cabral,[†] Adriana Valério,[‡] Sérgio L. Morelhão,*[,‡] Noemi R. Checca,[§] Márcio M. Soares,[∥] and Cláudio M. R. Remédios[⊥]

[†]Universidade Federal do Oeste do Pará, Santarém, Pará, Brazil

[‡]Institute of Physics, University of São Paulo, São Paulo, 05508-090 São Paulo, Brazil

[§]Brazilian Center for Research in Physics-CBPF, Rio de Janeiro, Rio de Janeiro, Brazil

[∥]Brazilian Synchrotron National Laboratory-LNLS/CNPEM, Campinas, São Paulo, Brazil

[⊥]Instituto de Ciências Exatas e Naturais, Universidade Federal do Pará, Belém, Pará, Brazil

Supporting Information

ABSTRACT: In situ synchrotron X-ray powder diffraction is used to elucidate the formation mechanism of multiferroic $BiFeO_3$ nanoparticles during moderate heat treatment at ambient pressure of an amorphous precursor. A wet chemical synthesis is used to obtain the precursor, formed after solvent elimination of an aqueous solution containing iron and bismuth nitrates and tartaric acid. The in situ experiments are performed at two reaction temperatures and two heating rates, both giving rise to the growth of $BiFeO_3$ nanoparticles without going through any intermediate crystalline phases. A detailed XRD line profile intensity analysis as a function of time and temperature provides information on the nucleation rate, growth kinetics, and size distribution of the nanoparticles.

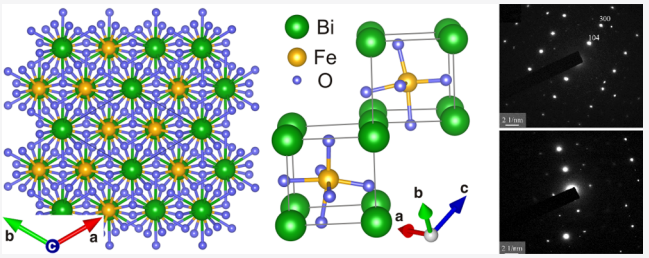

INTRODUCTION

Harmonic nanoprobes for biomedical imaging[1−5] have motivated much of the recent research in bismuth ferrite nanoparticles.[6−8] $BiFeO_3$ (or simply BFO) is also one of the most widely studied multiferroic materials, as it is both magnetic and a strong ferroelectric at room temperature:[9] antiferromagnetic ordering with a reasonably high Néel temperature (≲370 °C, depending on crystallite size)[10] and ferroelectric ordering with a high Curie temperature (∼825 °C).[11−13] Applications in multifunctional devices,[14] spintronics,[15−17] nonvolatile memory,[18−20] energy harvesting,[21,22] and optoelectronics[23] are other innovative technologies seeing in BFO a nearly ideal candidate. Nonlinear optical nanocrystals for harmonic generation offer a few advantages over existing bioimaging techniques. Tunable frequency within reasonable ranges (a very important ability for biomedical applications), long-term observation,[1,5] and, in the case of BFO, low cytotoxicity combined with singular optical and magnetic properties.[8,24] The wide use of BFO nanoparticles is, however, still inhibited by the difficulty in finding scalable synthesis routes to yield monodisperse ensembles of monocrystalline nanoparticles. There are many synthesis methods in the literature that describe the synthesis of BFO nanoparticles, although phase purity, size control, and dispersion often fall within the category of major challenges.[25−27] Wet chemical methods are quite attractive for being relatively simple and allowing controlled sizes of well-dispersed nanoparticles.[28−30] In particular, a promising wet chemical method follows a facile synthesis route based on solvent evaporation and tartaric acid as a chelating agent.[31] It provides monocrystalline single-phase BFO nanoparticles at a relatively low temperature (<500 °C), without formation of intermediate or secondary phases.[8,27,28]

Optimization of synthesis procedures for controlling phase purity and manipulating the size and size distribution of nanoparticles requires adequate tools to study the growth kinetics. Synchrotron X-ray diffraction (SXRD) has been used to investigate and elucidate the formation and growth of nanocrystals in general,[32−36] as well as of BFO nanocrystals prepared by high-temperature, high-pressure aqueous solutions of metal salts.[37] Nevertheless, an understanding of the formation and growth of BFO nanocrystals from amorphous precursors is still lacking, which is necessary for scalable production methods via promising wet chemical routes. In this work, in situ SXRD is used to monitor the phase purity and growth kinetics from an amorphous precursor to crystalline BFO nanoparticles during heating ramps and for different annealing temperature plateaus. The results lead to a parametric equation describing crystallite sizes as a function of time and temperature. Semiquantitative data analysis is

Received: July 9, 2019
Revised: December 10, 2019
Published: December 20, 2019

DOI: 10.1021/acs.cgd.9b00896
Cryst. Growth Des. 2020, 20, 600−607

performed to elucidate the temporal evolution of nanoparticle population during nucleation and coarsening. Time-dependent crystallite size distributions are proposed to describe size dispersion in BFO nanoparticle systems.

EXPERIMENTAL SECTION

Material Preparation. Stoichiometric amounts of $Bi(NO_3)\cdot 5H_2O$ and $Fe(NO_3)_3\cdot 9H_2O$ were dissolved in 2 N HNO_3 solution by vigorous magnetic stirring. After the total dissolution of metal nitrates, tartaric acid was added to the solution in a 1:1 molar ratio with respect to metal nitrates. The resulting mixture was heated to nearly 70 °C with continuous stirring on a hot plate until the elimination of the solvent and thus formation of the precursor material.

In Situ Analysis. Synchrotron X-ray diffraction was performed in the multidetector powder diffractometer of the XRD1 beamline at the Brazilian Synchrotron Light Laboratory (LNLS).[38,39] The acquisition time was 38 s for each diffraction pattern with subsequent correction by the reference signal from the incident beam monitoring system. Monochromatic 12 keV X-rays were used, exact wavelength λ = 1.033012 Å, as calibrated by using a silicon NIST standard. It also provides the instrumental peak broadening $\beta_{inst}(2\theta) = 0.0294° + 2\theta/3655$ for $2\theta < 50°$ and diffractometer offset correction in 2θ (<0.00005°). The precursor material was placed inside a glass capillary with a diameter of 0.3 mm, and the glass capillary was fixed in ferromagnetic stainless steel holders for heating by a hot air flow, with Gas Blower GSB 1300 (FMB Oxford) equipment. The air temperature T at the sample position was measured by a thermocouple prior to the experiment, leading to $T = 0.879T_{gas} + 1.32$ °C, where T_{gas} is the nominal value at the gas blower system.

Electron Microscopy. Transmission electron microscopy (TEM) and selected area electron diffraction (SAED) were conducted in a JEOL 2100F instrument, operating with 200 keV electrons and a 112 μA beam current. It is equipped with a 11 megapixel CCD camera (GATAN Orius). SAED patterns were acquired under similar aperture and camera length conditions.

RESULTS AND DISCUSSION

Figure 1 shows the in situ crystallization analysis of the precursor material under two different thermal treatments (inserts). In Figure 1a, the sample undergoes heating at a uniform rate of 5 °C/min (nominal value) until diffraction peaks start to emerge at the end of the heating ramp (red-yellow circle at the inset). Further crystallization and growth takes place at the annealing temperature T = 400 °C for about 120 min, after which the sample is cooled at a rate of 10 °C/min (nominal) until nearly room temperature. In Figure 1b, the crystallization begins with heating, $T \simeq 384$ °C (red-yellow circle at the inset), and continues at higher temperatures for 168 min, being 67 min still with heating and 101 min at T = 500 °C. In both processes, BFO nanocrystals are obtained in a single step without intermediate crystalline phases, such as the Bi_2O_3 phase observed to form before the $BiFeO_3$ nanocrystals during synthesis via an aqueous solution of $Bi(NO_3)_3$ plus $Fe(NO_3)_3\cdot 9H_2O$, using KOH as a mineralizer agent.[37] Also, no signals of residual phases are present, as seen when similar routes are used with different chelating agents.[8,28]

A detailed data analysis was performed on each SXRD pattern by adjusting the line profile of a few previously selected diffraction peaks (Figure 2a,d). This strategy of individually adjusting each diffraction peak instead of adjusting full patterns was chosen to ensure the best possible fit of each region of interest in each pattern of the hundreds analyzed here. Moreover, to improve accuracy in extracting

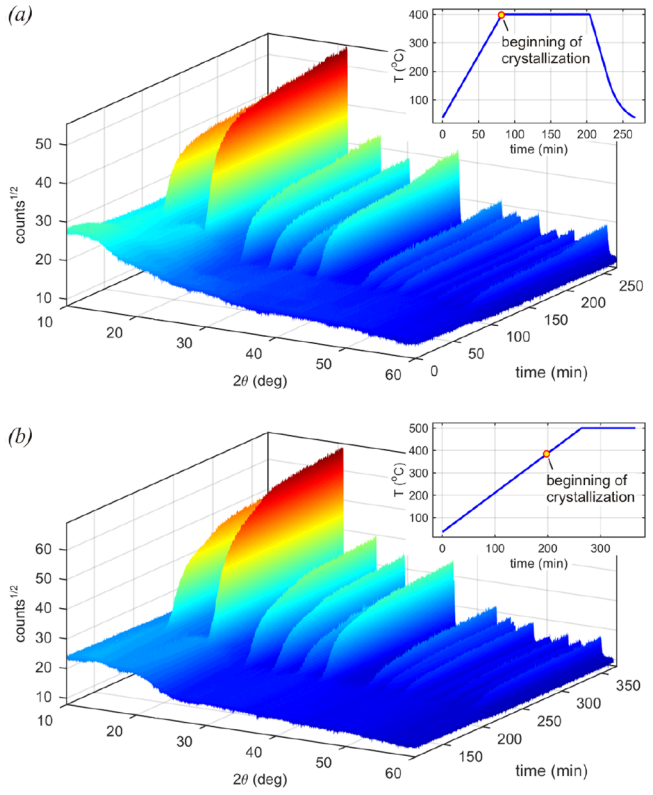

Figure 1. In situ SXRD analysis of BFO nanoparticle synthesis as a function of time and temperature T. Thermal treatments are shown as insets. (a) Fast heating (nominal 5 °C/min), crystallization, 120 min of annealing at a steady temperature of T = 400 °C, and cooling. (b) Slow heating (nominal 2 °C/min), crystallization with heating, and 101 min of annealing at the steady temperature T = 500 °C. Diffraction peaks are emerging (beginning of crystallization) at the time instant and temperature indicated in the insets (red-yellow circles). Only one phase is present at any instance of time in both syntheses.

diffraction peak positions, peak widths (fwhm), and integrated intensities (peak area above background), the number of adjustable parameters was minimized by choosing simple fitting functions that works for all patterns obtained along the synthesizing processes. Fitting parameters were adjusted by a genetic algorithm,[40] and the background around each peak was adjusted by linear interpolation. Figure 2 shows examples of line profile fitting with Gaussian functions of the diffraction peaks obtained at the beginning of crystallization and at the end of heating (Figure 1b). The success of the chosen method of data analysis in terms of fit quality and reliability during both processes can be verified in Figure 3, where values related to peak positions, widths, and integrated intensities exhibit very consistent behaviors with a minimum of random dispersion among themselves, revealing clear trends as a function of time and temperature. Only the values related to the peak widths of weak reflections, 006 and 202, show greater dispersion than the other values, making clear that low signal to noise ratio compromises first the reliability of width measurements.

From the peak positions in 2θ, atomic interplane distances, $d = \lambda/2 \sin\theta$, are obtained and presented in Figure 3a,d as $\Delta d/d$ for the sake of comparison. The d-spacing values confirm the steady temperatures during annealing, as well as the constant heating rate soon after the beginning of

DOI: 10.1021/acs.cgd.9b00896
Cryst. Growth Des. 2020, 20, 600−607

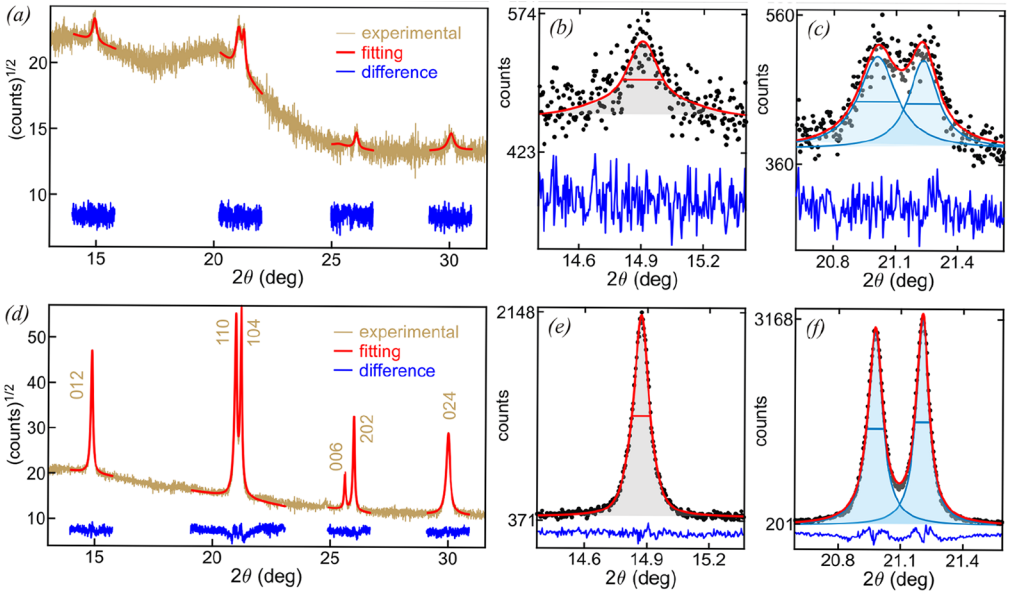

Figure 2. Line profile fittings of BFO diffraction peaks in Figure 1b. (a–c) At the beginning of crystallization, time 198 min, and T = 384 °C. (d–f) At the end of the heating ramp, time 264 min and T = 500 °C. A genetic algorithm is used to adjust the fitting curves (solid red lines) given either by one or two Gaussian functions, as detailed in (b, c) and (e, f); horizontal lines stand for peak widths (fwhm), while shaded areas stand for integrated intensities above the background. Difference curves (solid blue lines) are shown below all peaks. *hkl* reflection indexes are indicated aside each peak in (d).

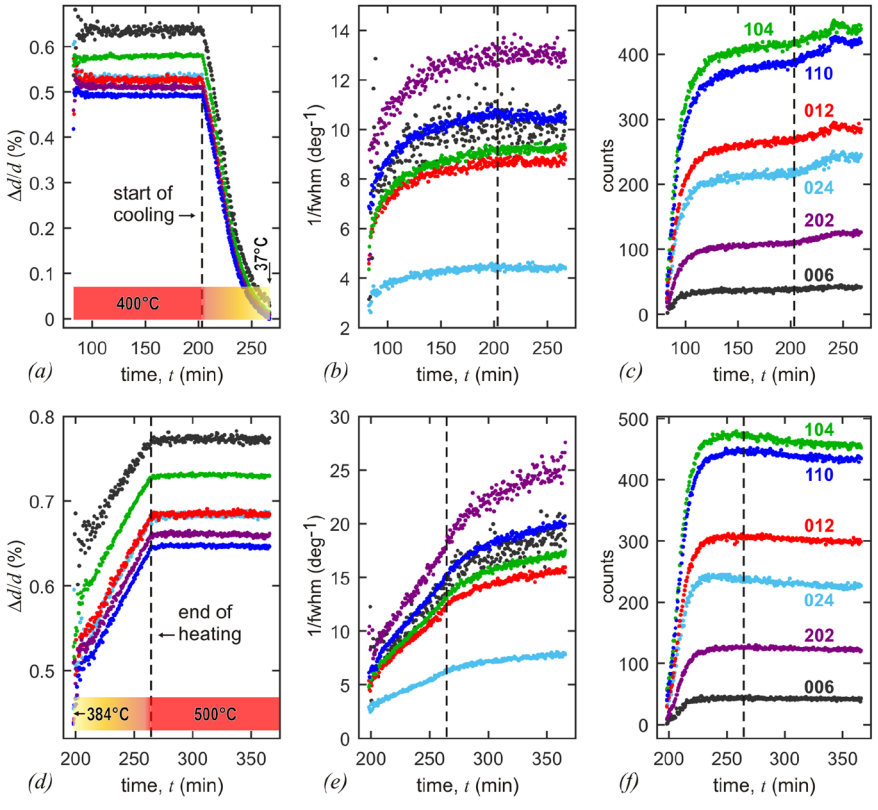

Figure 3. Extracted values (dots) from line profile fitting of the main diffraction peaks of BFO during crystallization (a–c) from the crystallization in Figure 1a and (d–f) from the crystallization in Figure 1b. (a, d) Variation in d spacing regarding bulk values[41] at room temperature. (b, e) Peak widths (fwhm) deconvolved from instrumental broadening $\beta_{inst}(2\theta)$ and shown as 1/fwhm for the sake of clarity. (c, f) Integrated intensities (peak area above background). *hkl* reflection indices are indicated by colors as in (c, f). Instants of times (vertical dashed lines) when cooling starts (a–c) or heating ends (d–f) are also indicated in either process, as well as color bars for temperature in (a, d).

crystallization in Figure 3d. Lattice parameters a and c as a function of temperature were determined by linear interpolation of the mean d-spacing values from reflections 110 and 006 at steady temperatures: at 400 °C (from 100 to 160

DOI: 10.1021/acs.cgd.9b00896
Cryst. Growth Des. 2020, 20, 600–607

min in Figure 3a) d_{110} = 2.80314 ± 0.00005 Å and d_{006} = 2.32621 ± 0.00016 Å and at 500 °C (from 280 to 340 min in Figure 3d) d_{110} = 2.80746 ± 0.00003 Å and d_{006} = 2.32943 ± 0.00007 Å. As $a = 2d_{110}$ and $c = 6d_{006}$, these values lead to

$$a(T) = 5.6063\ \text{Å} + \kappa_a(T - T_0) \text{ and}$$
$$c(T) = 13.957\ \text{Å} + \kappa_c(T - T_0) \quad (1)$$

where $\kappa_a = (8.65 \pm 0.04) \times 10^{-5}$ Å/°C, $\kappa_c = (19.3 \pm 0.1) \times 10^{-5}$ Å/°C, T_0 = 400 °C, and ±0.5 °C was the accuracy attributed to the difference of 100 °C between the steady temperatures for which the thermal expansion coefficients κ_a and κ_c were calculated. This linear approach for $a(T)$ and $c(T)$ provides a good agreement to all data above the crystallization temperature, 384 °C $\lesssim T \leq$ 500 °C; see section S1 in the Supporting Information for detailed comparisons of eq 1 also with the data acquired during heating and cooling. At the first 5 min of growth, time ≃200 min in Figure 3d, expansion coefficients are much higher than those described in eq 1. This fact has also been reported by other authors and attributed to the behavior of small particles in which the rhombohedral structure of BFO tends to be a cubic perovskite structure.[10,37]

Peak widths provide an estimation of crystallite size (size of small crystals or particles diffracting in powder samples) when they are deconvolved from instrumental broadening β_{inst}, according to $\beta_s = (\beta_{exp}^2 - \beta_{inst}^2)^{1/2}$, where β_{exp} stands for the actual fwhm extracted by line profile fitting. In the absence of strain and other lattice imperfections, the Scherrer equation[42] for crystallites of dimension $R_g = 0.46\lambda/\beta_s \cos\theta$, can be applied directly to the β_s values presented in Figure 3b,e. The dimension R_g stands for the apparent radius of gyration from the perspective of a given reflection;[43] for instance, spheres of diameter D have $R_g = D\sqrt{3/20}$ and cubes of side L have $R_g = L/2$. In both crystallization processes and at any instant of time, Bragg reflections with respect to orthogonal directions of the unit cell, in particular the 110 and 006 reflections have practically the same widths, while reflection 202 along the diagonal 101 direction is narrower by nearly $1/\sqrt{2}$. These facts led us to estimate crystallite sizes based on particles of cuboid shapes of edge $L_s = 2R_g = 0.92\lambda/\beta_s \cos\theta$, as also assumed by other authors.[8,31,44] As reflection 110 led to values of peak width with much better statistics than reflection 006, the particle sizes reported in Figure 4 were obtained from peak fitting of reflection 110.

In the case of reflections with the same apparent radius of gyration, their widths have to present variation only with the $1/\cos\theta$ factor. Lattice imperfections can also affect the reflection widths, but their presence is strikingly evident only for reflection 024, whose width is about twice that expected by the $1/\cos\theta$ rule. This excessive broadening of reflection 024 occurs in both crystallization processes (Figure 3b,e) and even after cooling (see also the Rietveld analysis in section S1 in the Supporting Information), clearly showing that the d spacing along this direction can be under strain or the lattice coherence of 024 Bragg planes has been affected by planar defects such as stacking faults or twinning.[45,46]

Under steady temperatures, particle size as a function of time can be reproduced by the simple parametric equation

$$L_s(t) = L_f(T)[1 - e^{-(t-t_0)/\tau}] \quad (2)$$

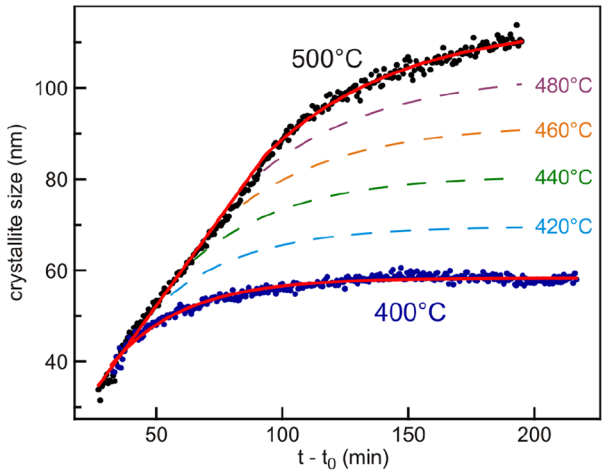

Figure 4. Experimental (dots) and adjusted (solid red lines) values of crystallite size L_s as a function of time in both crystallization processes at 400 °C (t_0 = 50.6 min) and at 500 °C (t_0 = 171 min). Values are based on the peak width of reflection 110 and fitting parameters given in Table 1. Other size values (dashed lines) from eq 2 for intermediate annealing temperatures and heating rate of 2 °C/min are also shown.

as seen in Figure 4 with the parameters in the first and second rows of Table 1. The constant growth rate observed during heating is also reproducible by eq 2 when a linear variation of the parameters previously determined for both steady temperatures is used: that is, $L_f(T) = 58.4 + 0.56(T - T_0)$ nm, $\tau(T) = 28.8 + 0.25(T - T_0)$ min, and T_0 = 400 °C. To combine both solutions, that during heating and that under steady temperature, t_0 has to vary linearly from an empirical value of t_0 = 171 to 191 min, third row of Table 1, that is t_0 in eq 2 being replaced by $t_{0,h}(T) = 171 + 0.2(T - T_0)$ min during heating. For the purpose of comparing the crystallization processes, particle sizes in Figure 4 were plotted as a function of $t - t_0$, where t_0 = 50.6 min for the former crystallization process (Figure 3b) and t_0 = 171 min for the latter process (Figure 3e). Although t_0 has been adjusted independently for each process, the curves of sizes in Figure 4 met each other at the beginning of both crystallization processes where $t - t_0 \simeq 37$ min. By changing the final temperature T in $L_f(T)$, $\tau(T)$, and $t_{0,h}(T)$, the curves of sizes vary smoothly between the experimental curves, from 400 to 500 °C, as shown for a few intermediate temperatures in Figure 4. To use these hypothetical curves as reliable predictions of particle sizes during crystallization processes

Table 1. Parameters Used in Eq 2 for Reproducing the Crystallite Sizes as a Function of Time t, As Shown in Figure 4

growth regime	L_f (nm)	τ (min)	t_0 (min)
steady T = 400 °C (t > 82.5 min in Figure 3b)	58.37 ± 0.01	28.8 ± 0.1	50.6 ± 0.7
steady T = 500 °C (t > 264.6 min in Figure 3e)	114.70 ± 0.03	53.82 ± 0.02	190.9 ± 0.1
ramp T: 400 °C → 500 °C (t: 207.7 → 264.6 min in Figure 3e)	58.37 → 114.7	28.8 → 53.82	171 → 191

DOI: 10.1021/acs.cgd.9b00896
Cryst. Growth Des. 2020, 20, 600−607

with a ramp of 2 °C/min and annealing temperature T, further investigation is necessary.

Integrated intensities in Figure 3c,f are saturating: that is, reaching maximum values while particles are still growing. It is more evident in the case of crystallization at 500 °C where saturation occurs around 250 min in Figure 3f, but diffraction peak widths continue to narrow after 250 min in Figure 3e. Within the kinematical theory of X-ray diffraction, saturation of integrated intensities indicates that the total volume of diffracting particles is stabilizing. Coarsening (particles growing in size) under a constant volume of diffraction is possible at the cost of small particles that dissolve providing material to larger ones in a process widely known as the Ostwald ripening phenomenon.[37,47] Since first described by Wilhelm Ostwald in 1896,[48] the phenomenon has been observed in a number of general nanocrystal growth systems where a broad spectrum of particle sizes is present.[49,50]

The slight rise of integrated intensities during cooling (Figure 3c for t > 200 min) is a direct consequence of a reduction in atomic thermal vibrations at lower temperatures, as also evidenced by Rietveld refinement (section S1 in the Supporting Information). The smooth fall of integrated intensities during annealing at 500 °C, mainly for strong reflections in Figure 3f, t > 260 min, can be caused by a combination of effects such as size-dependent changes in the randomness of the spatial crystallite misorientation and X-ray dynamical diffraction effects (absorption and rescattering) becoming significant in the ensemble of diffracting particles. Because of the transmission diffraction geometry in a spinning capillary, as well as the fall smoothness, changes in the misorientation randomness seem unlikely. As the main effect of dynamical diffraction (or primary extinction) is to diminish integrated intensities of large particles,[43] other weighted values by the intensity contribution from crystallites of different sizes in a powder sample can also be affected by primary extinction, such as the particle sizes obtained from peak widths.[51] Although the observed diminishing of integrated intensity is consistent with primary extinction, it is too small to imply in significant corrections in the obtained values of crystallite sizes (sections S3 and S4 in the Supporting Information).

In general, crystallites with dimensions in nanoscales, also called nanocrystals, have integrated intensities proportional to their volume V_c, following the so-called kinematic diffraction regime. In powder samples with particle size distribution (PSD) given by $n(t,L)$, the integrated intensity P of the diffraction peak $I(2\theta)$ is proportional to the total volume V of diffracting particles

$$P = \int I(2\theta)\, \mathrm{d}2\theta = K \int V_c(L) n(t, L)\, \mathrm{d}L = KV \tag{3}$$

K contains all terms that are independent of particle size L, and

$$N(t) = \int n(t, L)\, \mathrm{d}L \tag{4}$$

is the population of diffracting particles at the time instant t. It is convenient for the following discussion to write the PSD as $n(t, L) = N(t)\overline{n}(t,L)$ where $\int \overline{n}(t,L)\, \mathrm{d}L = 1$.

In situ measurements of integrated intensities during the growth of crystalline particles provide a direct route to access fluctuation in the population of particles. The predominance of either nucleation ($\mathrm{d}N/\mathrm{d}t > 0$) or Ostwald ripening ($\mathrm{d}N/\mathrm{d}t < 0$) processes can be evidenced from the experimental integrated intensity $P(t)$ when it is compared to the theoretical $P_0(t) = KN_0 \int V_c(L)\overline{n}(t,L)\, \mathrm{d}L$ values for PSDs with a constant number N_0 of particles and with imposed constraints to the determined $L_s(t)$ particle sizes from the Scherrer equation. In other words, when the peak width and integrated intensity values can both be reproduced by time-dependent PSDs with a constant number of particles ($\mathrm{d}N/\mathrm{d}t = 0$), the only effective mechanism of crystallization in action is size growth (coarsening) without further nucleation and without dissolution of small particles (Ostwald ripening). It is also possible that, when $\mathrm{d}N/\mathrm{d}t = 0$, nucleation and dissolution processes undergo a balance situation where the population of diffracting particles remains constant. Beyond this balance situation, toward $\mathrm{d}N/\mathrm{d}t < 0$, nucleation ends when it is overcome by dissolution, as nucleation and Ostwald ripening are exclusive processes that can not coexist locally in the same region of the sample. The chemical potential on the surface of large particles, capable of dissolving small particles, is also capable of suppressing the nucleation process.

The relative fluctuation in particle population is given by $N(t)/N_0 = P(t)/P_0(t)$, where $P(t')$ defines the initial population, $N_0 \propto P(t') = P_0(t')$, at the time instant t' when the crystallization begins according to the detection capability of the X-ray diffraction system. In the first crystallization, Figure 1a or Figure 3a–c, t' = 82.5 min. In the second crystallization, Figure 1b or Figure 3d–f, t' = 198 min. By using log-normal PSDs[52,53] and the integrated intensities from reflection 110, the relative fluctuations $N(t)/N_0$ of particle population during both crystallization processes were obtained as shown in Figure 5. The $N(t)/N_0$ curves as well as their

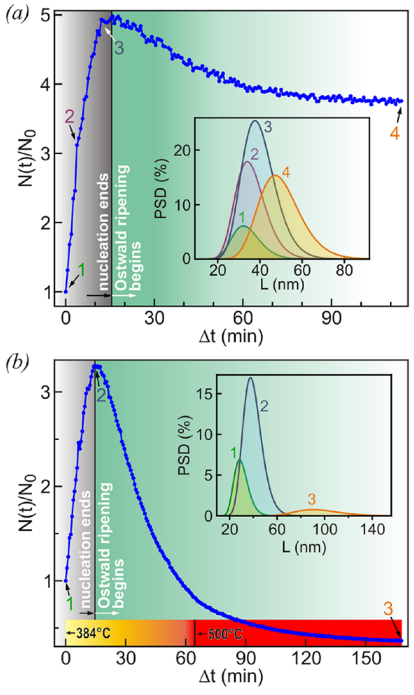

Figure 5. Relative fluctuation $N(t)/N_0$ in nanoparticle population during synthesis. (a) Synthesis at 400 °C (Figure 3b,c). (b) Synthesis under heating and annealing at 500 °C (Figure 3e,f), as indicated at the bottom by a color bar for temperature. In both syntheses, $\Delta t = t - t' = 0$ regards the instant when diffraction peaks become observable. Log normal PSDs at the time instants indicated by numbered arrows are shown in the insets.

DOI: 10.1021/acs.cgd.9b00896
Cryst. Growth Des. 2020, 20, 600–607

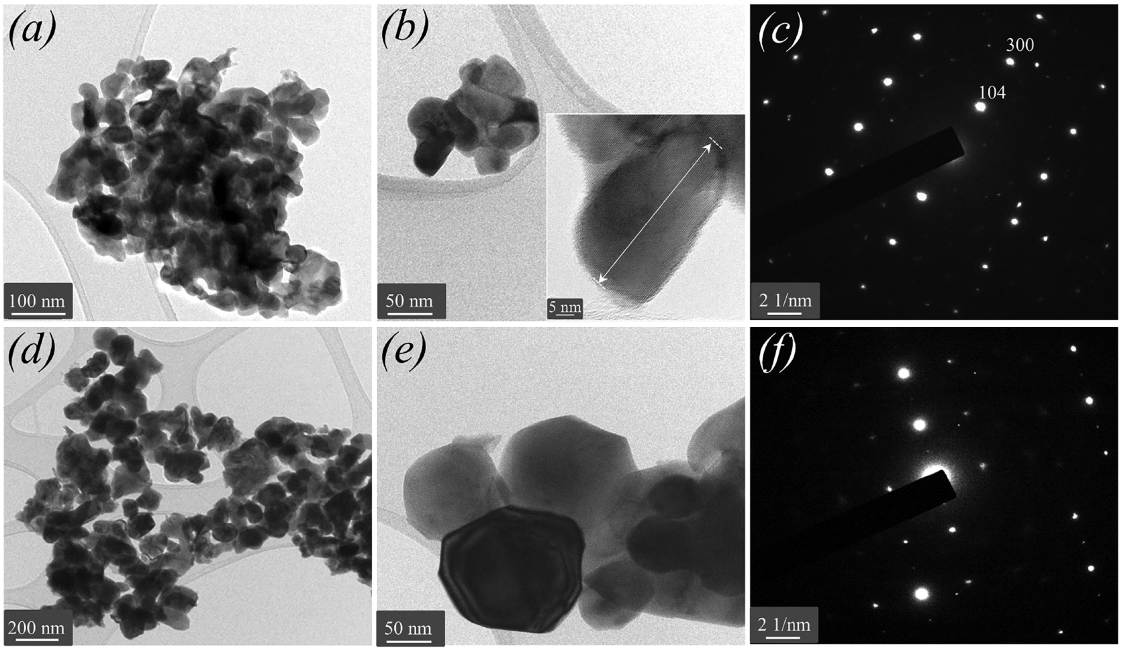

Figure 6. (a, b) TEM and (c) SAED of nanoparticles synthesized at 400 °C. (d, e) TEM and (f) SAED of nanoparticles synthesized at 500 °C.

derivatives, $dN(t)/dt$, are quite independent of PSD parameters such as mode (most probable size) L_0 and standard deviation in log scale σ, as far as these parameters are constrained to provide the observed particle sizes $L_s(t)$ in Figure 4. Snapshots of the used PSDs at different instants of time are shown in the insets of Figure 5.

There are countless PSDs leading to diffraction peaks with exactly the same width (section S4 in the Supporting Information). For log-normal PSDs with fixed σ, the time evolution of the PSD normalized term, $\overline{n}(t,L)$, follows a nearly linear relationship in which its mode is constrained to the particle size from the Scherrer equation as $L_0(t) \simeq f(\sigma)L_s(t)$. X-ray energy, Bragg reflection, and even dynamical diffraction effects change this $f(\sigma)$ factor (section S4 in the Supporting Information). To give a few examples when 12 keV X-rays and reflection 110 are used, $f(\sigma) \simeq 0.954$, 0.824, and 0.645 for σ = 0.1, 0.2, and 0.3, respectively. The $N(t)/N_0$ curves in Figure 5 were obtained by using PSDs with σ = 0.2 and $L_0(t) = 0.824L_s(t)$. The choice of larger or smaller values of σ implies a smaller or larger shift of L_0 during growth, but the $N(t)/N_0$ curves remain unchanged.

In situ analysis of both synthesizing processes reveals that nucleation ceases in about 15 min after the appearance of the diffraction peaks and that the particle sizes at this time instant are very similar: for instance, PSDs of mode $L_0 = 38 \pm 1$ nm in both cases (insets of Figure 5a,b). Beyond this point where $dN/dt = 0$, Ostwald ripening becomes the dominant process. For the synthesis initiated under heating followed by annealing at 500 °C, the maximum population of particles at the end of nucleation falls by a factor of 6.8 during the next 150 min. Further reduction seems possible for a longer period of times at 500 °C. On the other hand, for the synthesis at 400 °C, the maximum population falls by a factor of only 1.3, and the final population is almost stabilized, $dN/dt \rightarrow 0$, in about 90 min. Spontaneous ending of Ostwald ripening implies in PSD of limited spectrum of sizes in which the chemical potential at the surface of larger particles are no longer able to dissolve the smallest particles, at least for this temperature (400 °C) of a few degrees above the minimum temperature for initial nucleation (~384 °C).

Nucleation without significant coarsening is observed in the first 4 min of crystallization in Figure 5a, between points indicated by arrows 1 and 2, when the temperature after the fast heating (5 °C/min) may still be stabilizing inside the sample aimed at the plateau of 400 °C. In this interval with nucleation ratio of $dN/dt = 0.58$ min^{-1}, the initial population increases by a factor of 3.1 while the PSD mode undergoes a small shift from 32.0 to 34.1 nm (PSDs 1 and 2, inset of Figure 5a). After this fast nucleation, the ratio reduces to $dN/dt = 0.25$ min^{-1} at point 2 (Δt = 3.8 min), which is practically the same initial ratio of $dN/dt = 0.24$ min^{-1} (Δt < 2 min) of the crystallization process at higher temperature and slower heating ramp in Figure 5b. A similar increase in population, by a factor of 3.2, is also observed on heating, but during the whole nucleation stage where the shift of PSD mode is much larger, going from 28.6 to 37.7 nm (PSDs 1 and 2, inset of Figure 5b). Fast nucleation implies a spontaneous formation of crystallites until a certain size for a given steady temperature, above which both processes of nucleation and coarsening compete for consumption of the precursor material until Ostwald ripening begins to dominate. Fast nucleation without coarsening corresponds to step I in a nucleation mechanism recently discussed.[54] For the precursor used at ambient pressure, the temperature for fast nucleation seems to be slightly lower than 400 °C, but the heating rate may play a role.

Actual PSDs of samples synthesized at 400 and 500 °C, as well as their crystallinity, were investigated ex situ by electron microscopy. High-resolution TEM and SAED are presented in Figure 6, while the PSDs from several TEM images of each sample are shown in Figure 7. The particles have 3D shapes with facets and similar dimensions in orthogonal directions, the facets being more well-defined for larger particles as seen in Figure 6e. Samples were shown to be monocrystalline as the same crystal lattice extends throughout the particles, easily visible in Figure 6b (inset), and the spot patterns have clean

DOI: 10.1021/acs.cgd.9b00896
Cryst. Growth Des. 2020, 20, 600−607

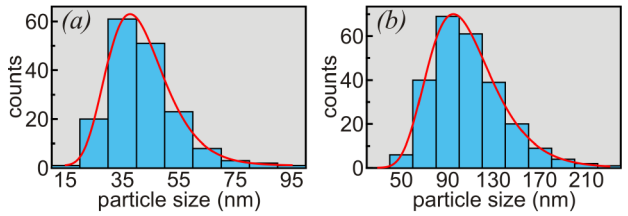

Figure 7. Particle size distributions (bars) from high-resolution TEM images and best-fitting log normal curves (solid-red lines). (a) Crystallization at 400 °C, L_0 = 37.3 nm, and σ = 0.264. (b) Crystallization at 500 °C, L_0 = 94.9 nm, and σ = 0.288.

arrays, without amorphous rings or multiple spots (many tiny spots instead of single ones). PSDs are well represented by log normal functions, and they are very compatible with those expected from in situ SXRD data analysis. Synthesis at 400 °C provides PSDs with a mode of around 40 nm, while at 500 °C PSDs have a mode at around 100 nm.

CONCLUSIONS

A promising synthesis route based on solvent evaporation and tartaric acid as a chelating agent has been shown to provide an appropriate amorphous precursor to the controlled production of monocrystalline, phase-pure $BiFeO_3$ nanoparticles. The controlled formation and growth of crystalline $BiFeO_3$ nanoparticles can be achieved by proper adjustment of the reaction temperature and annealing time. For harmonic bioimaging applications, nanoparticles with a minimum of size dispersion have optimum sizes of around 40 nm at the end of the nucleation process. Particle size distributions with modes above this value are possible at the cost of reducing the population of particles and increasing the dispersion of sizes due to growth by the Ostwald ripening process. As the nucleation process ends in about 15 min from the beginning of crystallization, customized procedures to scale up production of large amounts of monocrystalline, phase-pure nanoparticles may be envisaged. The detailed XRD line profile and intensity analysis as a function of temperature and time performed in this work also reveals that high temperatures favor size growth in detriment to the nucleation rate. It suggests another procedure to control size and size dispersion. By adjustment of reaction temperatures to a few degrees above the lowest temperature for nucleation to start, large populations of particles with sizes below 40 nm can be produced. This procedure is feasible since only the $BiFeO_3$ phase is formed from the precursor material used.

ASSOCIATED CONTENT

Supporting Information

The Supporting Information is available free of charge at https://pubs.acs.org/doi/10.1021/acs.cgd.9b00896.

Rietveld refinement, thermal expansion coefficients, XRD in powder samples with particle size distribution (PSD), dynamical diffraction corrections, and Scherrer equation for log-normal PSDs (PDF)

AUTHOR INFORMATION

Corresponding Author

*E-mail for S.L.M.: morelhao@if.usp.br.

ORCID

Sérgio L. Morelhão: 0000-0003-1643-0948

Author Contributions

A.J.F.C. and C.M.R.R. prepared the precursor material and carried out in situ X-ray diffraction measurements and Rietveld analysis. A.V., M.M.S., and S.L.M. contributed to the X-ray data analysis. N.R.C. carried out the electron microscopy experiments. The manuscript was written through contributions of all authors.

Notes

The authors declare no competing financial interest.

ACKNOWLEDGMENTS

The authors acknowledge the Brazilian Synchrotron Light Laboratory-LNLS and financial support from the Brazilian agencies CNPq (grant nos. 309867/2017-7 and 301061/2017-3), and CAPE S (grant no. 2018-5). N.R.C. also acknowledges the technical support from LABNANO/CBPF during electron microscopy work.

REFERENCES

(1) Le Xuan, L.; Zhou, C.; Slablab, A.; Chauvat, D.; Tard, C.; Perruchas, S.; Gacoin, T.; Villeval, P.; Roch, J.-F. Photostable Second-Harmonic Generation from a Single $KTiOPO_4$ Nanocrystal for Nonlinear Microscopy. *Small* **2008**, *4*, 1332−1336.

(2) Extermann, J.; Bonacina, L.; na, E. C.; Kasparian, C.; Mugnier, Y.; Feurer, T.; Wolf, J.-P. Nanodoublers as Deep Imaging Markers for Multi-Photon Microscopy. *Opt. Express* **2009**, *17*, 15342−15349.

(3) Pantazis, P.; Maloney, J.; Wu, D.; Fraser, S. E. Second Harmonic Generating (SHG) Nanoprobes for In Vivo Imaging. *Proc. Natl. Acad. Sci. U. S. A.* **2010**, *107*, 14535−14540.

(4) Dempsey, W. P.; Fraser, S. E.; Pantazis, P. SHG Nanoprobes: Advancing Harmonic Imaging in Biology. *BioEssays* **2012**, *34*, 351−360.

(5) Magouroux, T.; Extermann, J.; Hoffmann, P.; Mugnier, Y.; Le Dantec, R.; Jaconi, M. E.; Kasparian, C.; Ciepielewski, D.; Bonacina, L.; Wolf, J.-P. High-Speed Tracking of Murine Cardiac Stem Cells by Harmonic Nanodoublers. *Small* **2012**, *8*, 2752−2756.

(6) Schwung, S.; et al. Nonlinear Optical and Magnetic Properties of $BiFeO_3$ Harmonic Nanoparticles. *J. Appl. Phys.* **2014**, *116*, 114306.

(7) Schmidt, C.; Riporto, J.; Uldry, A.; Rogov, A.; Mugnier, Y.; Dantec, R. L.; Wolf, J.-P.; Bonacina, L. Multi-Order Investigation of the Nonlinear Susceptibility Tensors of Individual Nanoparticles. *Sci. Rep.* **2016**, *6*, 25415.

(8) Clarke, G.; Rogov, A.; McCarthy, S.; Bonacina, L.; Gun'ko, Y.; Galez, C.; Le Dantec, R.; Volkov, Y.; Mugnier, Y.; Prina-Mello, A. Preparation From a Revisited Wet Chemical Route of Phase-Pure, Monocrystalline and SHG-Effcient $BiFeO_3$ Nanoparticles for Harmonic Bio-Imaging. *Sci. Rep.* **2018**, *8*, 10473.

(9) Catalan, G.; Scott, J. F. Physics and Applications of Bismuth Ferrite. *Adv. Mater.* **2009**, *21*, 2463−2485.

(10) Selbach, S. M.; Tybell, T.; Einarsrud, M.-A.; Grande, T. Size-Dependent Properties of Multiferroic $BiFeO_3$ Nanoparticles. *Chem. Mater.* **2007**, *19*, 6478−6484.

(11) Kubel, F.; Schmid, H. Structure of a Ferroelectric and Ferroelastic Monodomain Crystal of the Perovskite $BiFeO_3$. *Acta Crystallogr., Sect. B: Struct. Sci.* **1990**, *46*, 698−702.

(12) Sosnowska, I.; Neumaier, T. P.; Steichele, E. Spiral Magnetic Ordering in Bismuth Ferrite. *J. Phys. C: Solid State Phys.* **1982**, *15*, 4835−4846.

(13) Palai, R.; Katiyar, R. S.; Schmid, H.; Tissot, P.; Clark, S. J.; Robertson, J.; Redfern, S. A. T.; Catalan, G.; Scott, J. F. β Phase and $\gamma-\beta$ Metal-Insulator Transition in Multiferroic $BiFeO_3$. *Phys. Rev. B: Condens. Matter Mater. Phys.* **2008**, *77*, No. 014110.

(14) Wu, J.; Fan, Z.; Xiao, D.; Zhu, J.; Wang, J. Multiferroic Bismuth Ferrite-Based Materials for Multifunctional Applications: Ceramic Bulks, Thin Films and Nanostructures. *Prog. Mater. Sci.* **2016**, *84*, 335−402.

DOI: 10.1021/acs.cgd.9b00896
Cryst. Growth Des. 2020, 20, 600−607

(15) Bibes, M.; Barthélémy, A. Towards a Magnetoelectric Memory. *Nat. Mater.* **2008**, *7*, 425−426.
(16) Balke, N.; Choudhury, S.; Jesse, S.; Huijben, M.; Chu, Y. H.; Baddorf, A. P.; Chen, L. Q.; Ramesh, R.; Kalinin, S. V. Deterministic Control of Ferroelastic Switching in Multiferroic Materials. *Nat. Nanotechnol.* **2009**, *4*, 868−875.
(17) Sando, D.; et al. Crafting the Magnonic and Spintronic Response of $BiFeO_3$ Films by Epitaxial Strain. *Nat. Mater.* **2013**, *12*, 641−646.
(18) Jang, H. W.; Ortiz, D.; Baek, S.-H.; Folkman, C. M.; Das, R. R.; Shafer, P.; Chen, Y.; Nelson, C. T.; Pan, X.; Ramesh, R.; Eom, C.-B. Domain Engineering for Enhanced Ferroelectric Properties of Epitaxial (001) BiFeO Thin Films. *Adv. Mater.* **2009**, *21*, 817−823.
(19) Yamada, H.; Garcia, V.; Fusil, S.; Boyn, S.; Marinova, M.; Gloter, A.; Xavier, S.; Grollier, J.; Jacquet, E.; Carrétéro, C.; Deranlot, C.; Bibes, M.; Barthélémy, A. Giant Electroresistance of Super-tetragonal $BiFeO_3$-Based Ferroelectric Tunnel Junctions. *ACS Nano* **2013**, *7*, 5385−5390.
(20) Heron, J. T.; et al. Deterministic Switching of Ferromagnetism at Room Temperature Using an Electric Field. *Nature* **2014**, *516*, 370−373.
(21) Choi, T.; Lee, S.; Choi, Y. J.; Kiryukhin, V.; Cheong, S.-W. Switchable Ferroelectric Diode and Photovoltaic Effect in $BiFeO_3$. *Science* **2009**, *324*, 63−66.
(22) Moubah, R.; Rousseau, O.; Colson, D.; Artemenko, A.; Maglione, M.; Viret, M. Photoelectric Effects in Single Domain $BiFeO_3$ Crystals. *Adv. Funct. Mater.* **2012**, *22*, 4814−4818.
(23) Qiao, L.; Zhang, S.; Xiao, H. Y.; Singh, D. J.; Zhang, K. H. L.; Liu, Z. J.; Zu, X. T.; Li, S. Orbital Controlled Band Gap Engineering of Tetragonal $BiFeO_3$ for Optoelectronic Applications. *J. Mater. Chem. C* **2018**, *6*, 1239−1247.
(24) Staedler, D.; et al. Cellular Uptake and Biocompatibility of Bismuth Ferrite Harmonic Advanced Nanoparticles. *Nanomedicine* **2015**, *11*, 815−824.
(25) Valant, M.; Axelsson, A.-K.; Alford, N. Peculiarities of a Solid-State Synthesis of Multiferroic Polycrystalline $BiFeO_3$. *Chem. Mater.* **2007**, *19*, 5431−5436.
(26) Silva, J.; Reyes, A.; Esparza, H.; Camacho, H.; Fuentes, L. $BiFeO_3$: A Review on Synthesis, Doping and Crystal Structure. *Integr. Ferroelectr.* **2011**, *126*, 47−59.
(27) Aguiar, E. C.; Ramirez, M. A.; Moura, F.; Varela, J. A.; Longo, E.; Simões, A. Z. Low-Temperature Synthesis of Nanosized Bismuth Eerrite by the Soft Chemical Method. *Ceram. Int.* **2013**, *39*, 13−20.
(28) Selbach, S. M.; Einarsrud, M.-A.; Tybell, T.; Grande, T. Synthesis of $BiFeO_3$ by Wet Chemical Methods. *J. Am. Ceram. Soc.* **2007**, *90*, 3430−3434.
(29) Yang, H.; Xian, T.; Wei, Z. Q.; Dai, J. F.; Jiang, J. L.; Feng, W. J. Size-Controlled Synthesis of $BiFeO_3$ Nanoparticles by a Soft-Chemistry Route. *J. Sol-Gel Sci. Technol.* **2011**, *58*, 238−243.
(30) Gao, T.; Chen, Z.; Zhu, Y.; Niu, F.; Huang, Q.; Qin, L.; Sun, X.; Huang, Y. Synthesis of $BiFeO_3$ Nanoparticles for the Visible-Light Induced Photocatalytic Property. *Mater. Res. Bull.* **2014**, *59*, 6−12.
(31) Ghosh, S.; Dasgupta, S.; Sen, A.; Sekhar Maiti, H. Low-Temperature Synthesis of Nanosized Bismuth Ferrite by Soft Chemical Route. *J. Am. Ceram. Soc.* **2005**, *88*, 1349−1352.
(32) Patzke, G. R.; Zhou, Y.; Kontic, R.; Conrad, F. Oxide Nanomaterials: Synthetic Developments, Mechanistic Studies, and Technological Innovations. *Angew. Chem., Int. Ed.* **2011**, *50*, 826−859.
(33) Mi, J.-L.; Clausen, C.; Bremholm, M.; Lock, N.; Jensen, K. M. ø.; Christensen, M.; Iversen, B. B. Rapid Hydrothermal Preparation of Rutile TiO_2 Nanoparticles by Simultaneous Transformation of Primary Brookite and Anatase: An in Situ Synchrotron PXRD Study. *Cryst. Growth Des.* **2012**, *12*, 6092−6097.
(34) Andersen, H. L.; Jensen, K. M. Ø.; Tyrsted, C.; Bøjesen, E. D.; Christensen, M. Size and Size Distribution Control of γ-Fe_2O_3 Nanocrystallites: An in Situ Study. *Cryst. Growth Des.* **2014**, *14*, 1307−1313.
(35) Birgisson, S.; Jensen, K. M. Ø.; Christiansen, T. L.; von Bülow, J. F.; Iversen, B. B. In Situ Powder X-Ray Diffraction Study of the Hydro-Thermal Formation of $LiMn_2O_4$ Nanocrystallites. *Dalton Trans.* **2014**, *43*, 15075−15084.
(36) Andersen, H. L.; Christensen, M. In Situ Powder X-Ray Diffraction Study of Magnetic $CoFe_2O_4$ Nanocrystallite Synthesis. *Nanoscale* **2015**, *7*, 3481−3490.
(37) Mi, J.-L.; Jensen, T. N.; Christensen, M.; Tyrsted, C.; Jørgensen, J. E.; Iversen, B. B. High-Temperature and High-Pressure Aqueous Solution Formation, Growth, Crystal Structure, and Magnetic Properties of $BiFeO_3$ Nanocrystals. *Chem. Mater.* **2011**, *23*, 1158−1165.
(38) Carvalho, A. M. G.; Araújo, D. H. C.; Canova, H. F.; Rodella, C. B.; Barrett, D. H.; Cuffni, S. L.; Costa, R. N.; Nunes, R. S. X-Ray Powder Diffraction at the XRD1 Beamline at LNLS. *J. Synchrotron Radiat.* **2016**, *23*, 1501−1506.
(39) Freitas Cabral, A. J.; Remédios, C. M. R.; Ospina, C. A.; Carvalho, A. M. G.; Morelhão, S. L. Structure of Antiferromagnetic NiO/Ferrimagnetic $NiMn_2O_4$ Composite Prepared by Sorbitol-Assisted Sol-Gel Method. *J. Alloys Compd.* **2017**, *696*, 304−309.
(40) Wormington, M.; Panaccione, C.; Matney, K. M.; Bowen, D. K. Characterization of structures from X-ray scattering data using geneti algorithms. *Philos. Trans. R. Soc., A* **1999**, *357*, 2827−2848.
(41) Palewicz, A.; Przeniosło, R.; Sosnowska, I.; Hewat, A. W. Atomic Displacements in $BiFeO_3$ as a Function of Temperature: Neutron Diffraction Study. *Acta Crystallogr., Sect. B: Struct. Sci.* **2007**, *63*, 537−544.
(42) Scherrer, P. Bestimmung der Gröbe und der Inneren Struktur von Kolloidteilchen Mittels Röntgenstrahlen. *Nachr. Ges. Wiss. Göettingen, Math.-Phys. Kl.* **1918**, 98.
(43) Morelhão, S. L. *Computer Simulation Tools for X-ray Analysis*; Springer International: Cham, Switzerland, 2016.
(44) Kaur, I.; Verma, N. K. Magnetic and Electric Properties of BFO−NFO Nanocomposites. *Mater. Sci. Semicond. Process.* **2015**, *33*, 32−35.
(45) Estevez-Rams, E.; Leoni, M.; Scardi, P.; Aragon-Fernandez, B.; Fuess, H. On the Powder Diffraction Pattern of Crystals with Stacking Faults. *Philos. Mag.* **2003**, *83*, 4045−4057.
(46) Morelhão, S. L.; Kycia, S. W.; Netzke, S.; Fornari, C. I.; Rappl, P. H. O.; Abramof, E. Dynamics of Defects in van der Waals Epitaxy of Bismuth Telluride Topological Insulators. *J. Phys. Chem. C* **2019**, *123*, 24818−24825.
(47) Ratke, L. Engineering Materials. In *Growth and Coarsening: Ostwald Ripening in Material Processing*; Springer-Verlag Berlin Heidelberg: 2002.
(48) Ostwald, W. *Lehrbuch der Allgemeinen Chemie*. **1896**, *2*, part 1.
(49) Zhang, Z.; Wang, Z.; He, S.; Wang, C.; Jin, M.; Yin, Y. Redox Reaction Induced Ostwald Ripening for Size- and Shape-Focusing of Palladium Nanocrystals. *Chem. Sci.* **2015**, *6*, 5197−5203.
(50) Rahaman, M. N. *Ceramic Processing and Sintering (Materials Engineering)*; CRC Press: 2003.
(51) Valério, A.; Morelhão, S. L.; Cabral, A. J. F.; Soares, M. M.; Remédios, C. M. R. X-Ray Dynamical Diffraction in Powder Samples with Time-Dependent Particle Size Distributions. *MRS Advances* **2019**, 1.
(52) Kiss, L. B.; Söderlund, J.; Niklasson, G. A.; Granqvist, C. G. New Approach to the Origin of Lognormal Size Distributions of Nanoparticles. *Nanotechnology* **1999**, *10*, 25−28.
(53) Cervellino, A.; Giannini, C.; Guagliardi, A.; Ladisa, M. Nanoparticle Size Distribution Estimation by a Full-Pattern Powder Diffraction Analysis. *Phys. Rev. B: Condens. Matter Mater. Phys.* **2005**, *72*, No. 035412.
(54) Bruno, M. A Two-Step Nucleation Model Based on Diffuse Interface Theory (DIT) to Explain the Non-Classical View of Calcium Carbonate Polymorph Formation. *CrystEngComm* **2019**, *21*, 4918−4924.

DOI: 10.1021/acs.cgd.9b00896
Cryst. Growth Des. 2020, 20, 600−607